AIAA AVIATION Forum
August 2-6, 2021, VIRTUAL EVENT
AIAA AVIATION 2021 FORUM

10.2514/6.2021-2108

Analysis of forced subsonic jets using spectral proper orthogonal decomposition and resolvent analysis

Liam Heidt * and Tim Colonius †
California Institute of Technology, Pasadena, CA USA

Akhil Nekkanti ‡ and Oliver T. Schmidt§
University of California San Diego, La Jolla, CA USA

Igor A. Maia¶ and Peter Jordan‖
Institute Pprime-CNRS-Université de Poitiers-ENSMA, Poitiers France

Various passive and active control strategies have been applied to turbulent jets and have achieved up to about a 5dB reduction in overall sound pressure level. However, the mechanisms by which forcing alters the turbulence and far-field sound are poorly understood. We investigate the effect of forcing by performing large-eddy simulations of turbulent axisymmetric jets subjected to periodic forcing at multiple frequencies and amplitudes. Spectral proper orthogonal decomposition is used to study the effect of the forcing on the linear spectrum. Low-frequency periodic forcing, with $St_f = 0.3$, while producing highly energetic tonal structures and noise, has a limited effect upon the underlying turbulent spectrum of the jet and the most energetic modes. High levels of forcing, 1% of the jet velocity, are required to achieve a small change to the turbulent mean flow and a minor shift in the turbulent spectrum. The changes in the overall spectrum and the shift in the modes are predicted well via the resolvent analysis performed on the new turbulent mean flow. This shows that the turbulent spectrum stems from the turbulent mean flow and not via interactions between phase-locked structures and the natural turbulence. High-frequency periodic forcing, with $St_f = 1.5$, is less effective at altering the mean flow field compared to the low-frequency forcing at the same amplitude, but results in a nonlinear interaction, potentially associated with vortex pairing, amplifying the turbulence spectrum at $St \approx 0.75$.

I. Introduction

Reducing the jet noise produced by tactical aircraft is made difficult by the impracticability of employing high-bypass-ratio engines that have vastly reduced the noise produced by commercial aviation aircraft. Instead, a number of methods have been devised to alter the flow in a more subtle manner. Both passive (chevrons, tabs, etc.) and active (fluidic injection, plasma actuators, etc.) control devices have been employed to reduce peak aft-angle radiation by as much as 5dB [1]. Active control devices are of particular interest as they avoid potential performance losses in mission-critical portions of the flight envelope where noise mitigation is not a critical issue. However, these passive and active control devices are designed empirically and generally lack a mechanistic understanding that would enable them to be scaled and improved.

Amongst studies seeking to characterize mechanisms, Kœnig et al. [2] studied a series of subsonic jets forced via a rotating center-body actuator that forces the jet with both a steady and unsteady component. They investigated two forcing frequencies, $St_f = 0.23, 0.46$, at an azimuthal mode number $m = 2$. Forcing the jet at $St_f = 0.23$ resulted in a broadband increase in noise production, whereas forcing at $St_f = 0.46$ resulted in a reduction in the noise produced by the jet. These results were interpreted in the context of what has become known as resolvent analysis [3–6], which

---

[*] PhD Student, Graduate Aerospace Laboratories of the California Institute of Technology, AIAA Student Member

[†] Frank and Ora Lee Marble Professor of Mechanical Engineering, Mechanical and Civil Engineering, Associate Fellow AIAA

[‡] PhD Student, Department of Mechanical and Aerospace Engineering, AIAA Student Member

[§] Assistant Professor, Department of Mechanical and Aerospace Engineering, Senior Member AIAA.

[¶] Post-Doctoral Research Fellow, Départment of Fluides Thermique et Combustion, Institute Pprime-CNRS-Université de Poitiers-ENSMA, Poitiers France.

[‖] Directeur de Recherche, Départment of Fluides Thermique et Combustion, Institute Pprime-CNRS-Université de Poitiers-ENSMA, Poitiers France.

regards the coherent turbulence as a forced response of the turbulent mean flow field. Actuation alters both the mean flow and introduces unsteady perturbations that can potentially be amplified by the mean flow. The parabolized stability equations were employed to show that the turbulent mean flow strongly amplified disturbances at the lower forcing frequency (and azimuthal mode number) but not at the higher one. Thus, the lower frequency forcing produced, in addition to an alteration of the mean flow, a strong, tonal unsteady response that led to a substantial increase in noise, whereas the higher frequency forcing led to an modification of the mean flow to one that was more stable, i.e., has lower amplification over a range of frequencies. This, in turn, led to an overall broadband noise reduction.

Similarly, Sinha et al. [7] investigated the effect of steady and periodic mass injection on the noise production of a supersonic, Mach 1.5, axisymmetric jet via the use of a spinning value actuator. They showed that the noise reduction observed was uniquely linked to the steady component of forcing employed. The unsteady forcing again resulted in a stabilized turbulent mean flow, but with the addition of highly energetic tones at the forcing frequency and its harmonics. These tones overwhelmed the broadband noise reduction. On the other hand, steady forcing (with the same mass flow rate) had a similar effect on the mean flow and produced the broadband noise reduction without the associated tones.

Therefore, these experimental studies suggest that noise reduction did not result from any direct interaction between the introduced disturbances and the background turbulence. Instead, it is a by-product of the generation of Reynolds stresses by the tonal disturbances (independent from those of the background turbulence) that deform the turbulent mean flow of the jet and thus alter the entire turbulence spectrum.

Recently, resolvent analysis and spectral proper orthogonal decomposition (SPOD) have been employed heavily in turbulent natural jets. SPOD [8–10] allows one to extract the energy spectra and decompose the flow into energy-ranked coherent structures. Good agreement has been found between structures seen in SPOD, generated via high-fidelity simulations [11, 12] and optimal modes generated via resolvent analysis [6]. Resolvent analysis has been used extensively to study subsonic, transonic, and supersonic jets [4, 6, 13] and has been used to develop low-rank jet models [6]. Recent work has expanded our understanding of instability mechanisms in natural jets by applying resolvent analyses to the full (non-parallel) turbulent mean flow field [6, 14]. Depending on the frequency and azimuthal mode number, the most amplified disturbances in the natural jet can differ from the Kelvin-Helmholtz (KH) modes and have been characterized as Orr modes [6] and streaks/lift-up mechanism [14]. Additionally, by introducing an eddy-viscosity model [13] (to close the nonlinear forcing term), the alignment between the SPOD and resolvent modes increases up to 90% at frequencies where the jet is low-rank.

The present work aims to understand how these most amplified disturbances are altered by forcing through both the direct linear effect (receptivity) and the changes to the corresponding mean flow. In addition, we seek to understand how nonlinear interactions amongst coherent structures are induced by higher-amplitude forcing and how forced structures compare to, and interact with, randomly-occurring coherent structures at harmonically coupled frequencies. We compute a series of high-fidelity LES of Mach 0.4, isothermal, turbulent, high-Reynolds number axisymmetric jets subjected to an annular periodic acoustic forcing. To understand the physics of the resulting flow, we pair these high-fidelity simulations of forced jets with resolvent analysis and SPOD.

II. Methods

A. Forced subsonic jet LES simulations

LES of isothermal Mach 0.4 forced jets are performed using the compressible flow solver "Charles" by Cascade Technologies. Recent results employing this scheme for natural results have led to sub-decibel agreement between the computational and experimental noise spectra [11] for all relevant angles and frequencies. A schematic of the simulation set-up is shown in figure 1. As in previous simulations, the jet nozzle is explicitly included in the computational domain, and synthetic turbulence is applied inside the nozzle to obtain a fully turbulent boundary layer. The jet has a Reynolds number, $Re_j = \rho_j U_j D/\mu_j = 4.5 \times 10^5$ and a Prandtl number of 0.7. The reader can find details on the numerical methods, subgrid-models, and meshing in Brès et al. [15]. The grid refinement is similar to Brès et al. [11], except that the annular refinement regions around the nozzle lip are expanded slightly to take into account the higher jet spreading rate expected with forced jets. In total, 19.2 million control volumes are employed.

The subscripts j and ∞ represent the jet and free-stream conditions, respectively. ρ is the density, μ is the viscosity, $M_j = U_j/c_j$ is the Mach number where c_j and U_j are the speed of sound, and natural jet mean flow velocity magnitude, respectively. Throughout this paper, variables are non-dimensionalized by U_j, jet diameter D, and pressure $\rho_j U_j^2$. Frequencies are reported with respect to the Strouhal number $St = fD/U_j$, where f is the frequency. The simulations were run with a computational time step $\Delta t D/c_\infty = 0.001$ and a total simulation time $t_{sim} D/c_\infty = 1000$ (after the initial transient, due to the forcing, has passed).

The simulation contains a coflow of $M_\infty = 0.009$ with an additional plane wave acoustic forcing applied in an annular region around the nozzle. The acoustic forcing is applied at a non-dimensional frequency $St_f = f_f D/U_j$ and amplitude a_0, where f_f is the forcing frequency. A schematic of the simulation set-up is shown in figure 1. The magnitude of the acoustic forcing applied along the co-flow boundary is scaled by the function $c(r)$, which results in the acoustic forcing decaying in an error function manner about $r = 5$. The acoustic forcing is defined by the following relations:

$$
\begin{aligned}
c(r) &= 0.5\big[1 - \mathrm{erf}\big(2(r-5)\big)\big],\\
u_f(r,t) &= a_0 sin(2\pi f_f t),\\
u_x(r,t) &= u_\infty + c(r) u_f(r,t),\\
u_r(r,t) &= u_\theta(r,t) = 0,\\
\rho(r,t) &= \rho_\infty + \rho_\infty (u_x(r,t) - u_\infty)/a_\infty,\\
p(r,t) &= p_\infty + a_\infty \rho_\infty (u_x(r,t) - u_\infty).
\end{aligned}
$$

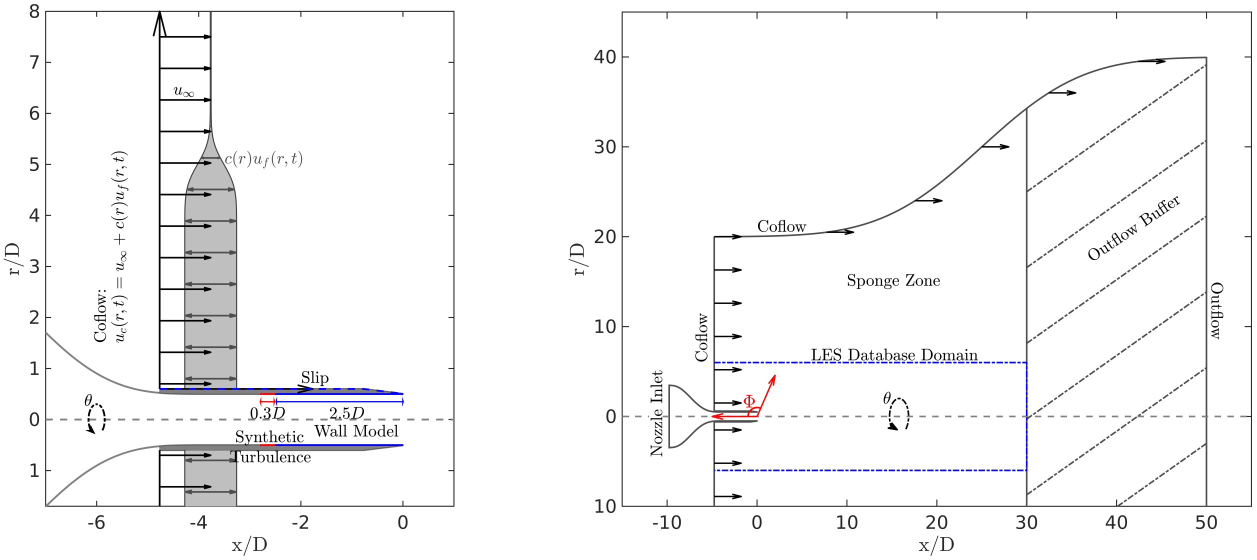

(a) Nozzle region schematic

(b) Full domain schematic

Fig. 1 LES simulation schematic, adapted from Brès et al. [11]

Along with the natural unforced jet (the LES database from Brès et al. [11] was employed), three simulations are run, two at $St_f = 0.3$ ($a_0/U_j = 1\%, 0.1\%$), and a higher frequency simulation at $St_f = 1.5$ ($a_0/U_j = 1\%$). In what follows, we refer to these as the low-frequency (LF) and high-frequency (HF) cases. The LF case was chosen to correspond to the frequency most commonly linked to the jet preferred mode [16], albeit uncertainty exists around this value [17], and experimental studies have suggested values from $St = 0.2 \longrightarrow 0.6$. The HF case was chosen as experimental studies [18, 19] have shown a broadband reduction in jet noise for both subsonic and supersonic jets at this frequency; although other frequency-azimuthal mode number pairs result in greater jet noise reduction.

LES databases' were saved for each computation at a set number of equispaced time points per forcing oscillation. For the LF computations, 48 steps per forcing oscillation were saved, whereas 12 steps per forcing oscillation were saved for the HF computation. This results in a Nyquist frequency of $St_N = 7.20$ and $St_N = 9.05$ for the LF and HF cases, respectively. The unstructured LES data was interpolated onto a structured cylindrical grid ($n_x \times n_r \times n_\theta = 656\times138\times128$) spanning $x \in [0, 30]$, $r \in [0, 6]$, and $\theta \in [0, 2\pi]$, which was employed in the subsequent SPOD analyses.

B. Resolvent analysis

Resolvent analysis relies on defining a linear operator for disturbances to the turbulent mean flow. We start with the following compact form of the time-independent, fully compressible continuity, Navier-Stokes, and energy equations,

$$\frac{\partial \boldsymbol{q}}{\partial t} = \boldsymbol{F}(\boldsymbol{q}), \tag{1}$$

where $\boldsymbol{q}$ is the state vector, and $\boldsymbol{F}$ is the flow operator. Next, we Reynolds-decompose the state vector, $\boldsymbol{q}$, into its long term mean, $\bar{\boldsymbol{q}}$, and the fluctuating component, $\boldsymbol{q}'$, shown by

$$\boldsymbol{q}(\boldsymbol{x}, \boldsymbol{r}, \boldsymbol{\theta}, \boldsymbol{t}) = \bar{\boldsymbol{q}}(\boldsymbol{x}, \boldsymbol{r}, \boldsymbol{\theta}) + \boldsymbol{q}'(\boldsymbol{x}, \boldsymbol{r}, \boldsymbol{\theta}, \boldsymbol{t}).$$

Substituting this decomposition into equation 1 and then separate terms that are linear and nonlinear with respect to the perturbation, $\boldsymbol{q}'$, results in

$$\frac{\partial \boldsymbol{q}'}{\partial t} - \boldsymbol{A}(\bar{\boldsymbol{q}})\boldsymbol{q}' = \boldsymbol{f}(\bar{\boldsymbol{q}}, \boldsymbol{q}'), \tag{2}$$

where $\boldsymbol{A}(\bar{\boldsymbol{q}})$ is the linearized governing equations and $\boldsymbol{f}(\bar{\boldsymbol{q}})$ contains all the nonlinear terms along with any additional system inputs. For resolvent analysis, these equations are discretized using previously developed methods [6]. The turbulent jets in this manuscript are round and, in the absence of forcing, statistically-stationary. In the presence of forcing, the jets will have a periodic, deterministic component, as well as a residual, random component associated with the turbulence that is uncorrelated with the forcing. Both motions can be described in the temporal/azimuthal Fourier domain and motivate the following form of the linearized governing equations

$$(\boldsymbol{A}_m - i\omega \boldsymbol{I})\boldsymbol{q}_{m,\omega} = \boldsymbol{f}_{m,\omega}, \tag{3}$$

where, $\omega = 2\pi St$ is the frequency and m is the azimuthal mode number. For brevity, we omit the prime, $(\cdot)'$, in all perturbation quantities. The resolvent operator is then defined as

$$\boldsymbol{R}_{m,\omega} = (\boldsymbol{A}_m - i\omega \boldsymbol{I})^{-1}.$$

The weighted resolvent operator can subsequently be defined as

$$\hat{\boldsymbol{R}}_{m,\omega} = \boldsymbol{W}_q^{1/2} \boldsymbol{R}_{m,\omega} \boldsymbol{W}_f^{-1/2}, \tag{4}$$

where the weighting matrices $W_q = W_f = W$ are defined via the compressible Chu energy norm [20]

$$\langle \boldsymbol{q}_1, \boldsymbol{q}_2 \rangle_E = \iiint \boldsymbol{q}_1^H \operatorname{diag}\left(\frac{\bar{T}}{\gamma \bar{\rho} M^2}, \bar{\rho}, \bar{\rho}, \bar{\rho}, \frac{\bar{\rho}}{\gamma(\gamma-1)\bar{T} M^2} \right) \boldsymbol{q}_2 r \mathrm{d}x \mathrm{d}r \mathrm{d}\theta = \boldsymbol{q}_1^H \boldsymbol{W} \boldsymbol{q}_2,$$

where, $(-)^H$ is the Hermatian transpose, M is the Mach number, and γ is the ratio of specific heats. $\boldsymbol{W}$ takes into account the energy and domain quadrature weights.

$\hat{\boldsymbol{R}}_{m,\omega}$ is then decomposed into the forcing and response modes that result in the highest gain via the singular value decomposition

$$\hat{\boldsymbol{R}}_{m,\omega} = \hat{\boldsymbol{U}}_{m,\omega}\boldsymbol{\Sigma}\hat{\boldsymbol{V}}^{H}_{m,\omega}. \tag{5}$$

The optimal forcing (left singular vectors) and response (right singular vectors) modes are $\boldsymbol{V}_{m,\omega} = \boldsymbol{W}_f^{-1/2}\hat{\boldsymbol{V}}_{m,\omega}$ and $\boldsymbol{U}_{m,\omega} = \boldsymbol{W}_q^{-1/2}\hat{\boldsymbol{U}}_{m,\omega}$, respectively. These modes are optimal in terms of the maximum energy gain, $\boldsymbol{\Sigma}$, between the forcing and response modes.

In this paper, the mean-flow consistent eddy-viscosity method of Pickering et al. [13] is employed to close the nonlinear forcing term. This results in vastly improved alignment between the SPOD and resolvent analysis modes across all relevant frequencies. This method relies on a Lagrangian optimization that determines the eddy viscosity field that minimizes the error by which the mean flow satisfies the axisymmetric zero-frequency linearized governing equations augmented with the addition of a eddy-viscosity model. For details on the optimization, we refer the reader to Pickering et al. [13]. The final eddy-viscosity field employed for the linearized Navier-Stokes (LNS) and resolvent analysis computations is scaled by a constant c. A single constant, $c \approx 0.11$, was employed for all four cases investigated in this paper. Similar to the results shown in Pickering et al. [13], this leads to improved alignment across the range of frequencies considered with only a small decrease in the alignment from the optimal coefficient $c(St_f)$. The eddy viscosity fields generated are all similar to the eddy viscosity fields shown in Pickering et al. [13] and thus are not shown for brevity.

C. Spectral Proper Orthogonal Decomposition

SPOD [8, 9] determines an optimal set of orthogonal modes that best represent the dataset. Unlike spatial only POD, these orthogonal modes express both the spatial and temporal correlation in the data. Recent work [10] has shown that SPOD combines the advantages of POD [21, 22] and dynamic mode decomposition [23], making it an ideal method to study turbulent jets. Additionally, recent work [4, 6, 10, 24] has shown a theoretical connection between resolvent analysis and SPOD.

We refer the reader to a review article [25] for details regarding the SPOD algorithm. In short, the time series at each point in space is segmented and Fourier transformed in time and azimuthal directions to produce a data matrix (for each discrete frequency, ω and azimuthal mode, m), $\boldsymbol{Q}_{m,\omega} = [\boldsymbol{q}^{(1)}_{m,\omega}, \boldsymbol{q}^{(2)}_{m,\omega}, \cdots, \boldsymbol{q}^{(ns-1)}_{m,\omega}, \boldsymbol{q}^{(ns)}_{m,\omega}]$, where ns is the number of segments (realizations). The SPOD modes $\boldsymbol{\Psi}_{m,\omega} = [\boldsymbol{\psi}^{(1)}_{m,\omega}, \boldsymbol{\psi}^{(2)}_{m,\omega}, \cdots, \boldsymbol{\psi}^{(ns-1)}_{m,\omega}, \boldsymbol{\psi}^{(ns)}_{m,\omega}]$ and energy $\boldsymbol{\Lambda}_{m,\omega} = \mathrm{diag}(\lambda^{(1)}_{m,\omega}, \lambda^{(2)}_{m,\omega}, \cdots, \lambda^{(ns-1)}_{m,\omega}, \lambda^{(ns)}_{m,\omega})$, at a given azimuthal mode number and frequency, are determined via the eigenvalue problem of the cross-spectral density matrix $\boldsymbol{S}_{m,\omega} = \boldsymbol{Q}_{m,\omega}\boldsymbol{Q}^H_{m,\omega}$ [8, 9]

$$\boldsymbol{S}_{m,\omega}\boldsymbol{W}\boldsymbol{\Psi}_{m,\omega} = \boldsymbol{\Psi}_{m,\omega}\boldsymbol{\Lambda}_{m,\omega}. \tag{6}$$

We note that the full cross-spectral density matrix is never formed; the SPOD modes can be constructed more efficiently through an SVD of the data matrix, or through an eigen-decomposition of the matrix $\boldsymbol{Q}^H_{m,\omega}\boldsymbol{W}\boldsymbol{Q}_{m,\omega}$.

Two decomposition frameworks are considered in this paper, the Reynolds decomposition and the triple decomposition, which are discussed in the next section.

D. Triple decomposition of forced jets

The natural jets considered in previous studies have been decomposed via the standard Reynolds decomposition,

$$\boldsymbol{q}(\boldsymbol{x},t) = \bar{\boldsymbol{q}}(x) + \boldsymbol{q}'(\boldsymbol{x},t). \tag{7}$$

In decomposing forced jets, particularly when the jet is forced via an external signal with a known phase, a useful framework is the Hussain and Reynolds triple decomposition [26–28]. Here, flow variables are decomposed into the mean (temporal average), a periodic component, and a turbulent component,

$$\boldsymbol{q}(\boldsymbol{x},t) = \bar{\boldsymbol{q}}(x) + \tilde{\boldsymbol{q}}(\boldsymbol{x},t) + \boldsymbol{q}''(\boldsymbol{x},t). \tag{8}$$

In literature, mixed terminology has been used to describe the last two components. We refer to the second term, $\tilde{\boldsymbol{q}}(\boldsymbol{x},t)$, linked to the external forcing, as the phase-locked component. The term $\boldsymbol{q}''(\boldsymbol{x},t)$ denotes the residual component as it represents the remainder between the original state and the temporal average and the phase-locked component. Additionally, the summation of the second and third terms is denoted as the total fluctuating component, $\boldsymbol{q}'(\boldsymbol{x},t)$. It is, by definition, equal to the fluctuating (or residual) component defined by the Reynolds decomposition. The temporal average term is defined as,

$$\bar{\boldsymbol{q}}(\mathbf{x}) = \lim_{T\to\infty} \frac{1}{T} \int_0^T \boldsymbol{q}(\boldsymbol{x},t)dt. \tag{9}$$

Additionally, the phase-average is defined as,

$$\langle \boldsymbol{q}(\mathbf{x},t)\rangle = \lim_{N\to\infty} \frac{1}{N} \sum_{n=0}^{N} \boldsymbol{q}(\mathbf{x},t+n\tau),$$

where, τ is the period of the external forcing. The phase-average for discrete snapshots is the average of all snapshots that correspond to the specific phase, ϕ, of the external forcing signal. The phase-locked component is then defined as the difference between the phase-average and the temporal average,

$$\tilde{\boldsymbol{q}}(\boldsymbol{x},t) = \langle \boldsymbol{q}(\mathbf{x},t)\rangle - \bar{\boldsymbol{q}}(\mathbf{x}). \tag{10}$$

Lastly, the residual component is defined as the difference between the original state vector and the phase-average,

$$\boldsymbol{q}''(\boldsymbol{x},t) = \boldsymbol{q}(\boldsymbol{x},t) - \langle \boldsymbol{q}(\mathbf{x},t)\rangle. \tag{11}$$

By definition of the temporal-mean and phase-average, the phase-locked and residual components are, on average, uncorrelated,

$$\overline{\boldsymbol{q}''(\boldsymbol{x},t)\tilde{\boldsymbol{q}}(\boldsymbol{x},t)} = 0. \tag{12}$$

Thus the triple decomposition helps separate the coherent structures that are phase-locked to the external forcing and coherent structures that are stochastic in nature that we shall identify through SPOD applied to the residual component.

III. Results

A. Mean flow

Figure 2 shows the centerline turbulent mean velocity magnitude. Additionally, the shear-layer momentum thickness, δ_θ, is presented in figure 3. Similar to previous studies, [11, 29], δ_θ is determined via

$$\delta_\theta(x) = \int_0^{r_{0.05}} \frac{\overline{u}_x(x,r)}{\overline{u}_x(x,0)} \left(1 - \frac{\overline{u}_x(x,r)}{\overline{u}_x(x,0)}\right) \mathrm{d}r,$$

where $\overline{u}_x(x,r)$ is the time and azimuthally averaged streamwise velocity. The radial bound on the integral, $r_{0.05}$, corresponds to the radial distance where $\overline{u}_x(x,r_{0.05}) - U_\infty = 0.05\,\overline{u}_x(x,0)$.

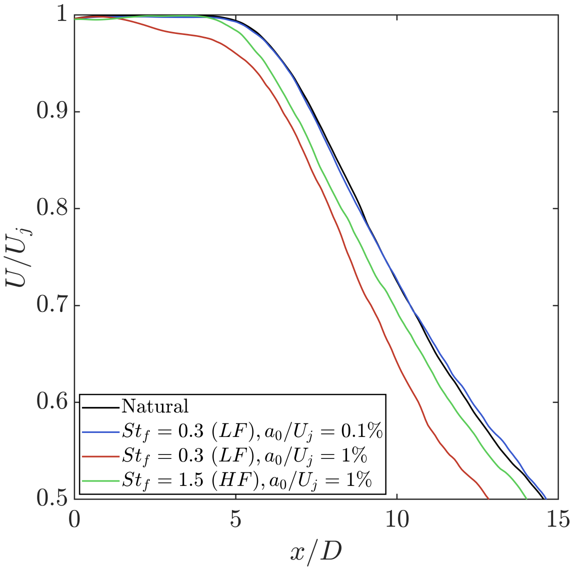

Fig. 2 Centerline axial velocity magnitude

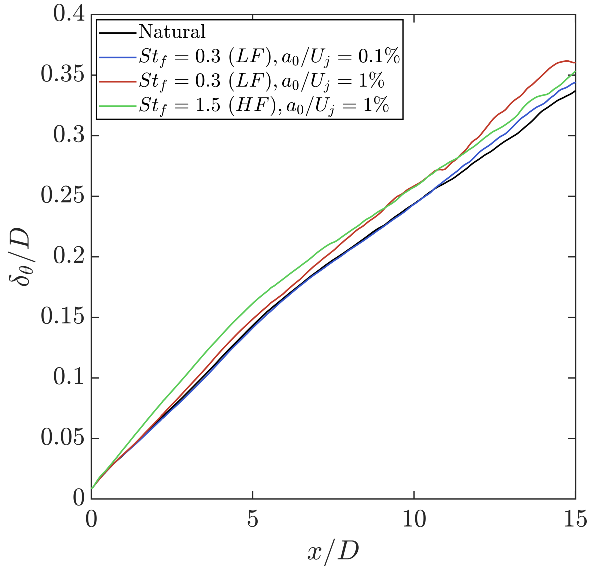

Fig. 3 Shear-layer momentum thickness

The two high-amplitude forcing cases result in significant change to the turbulent mean flow. The potential core length, defined as where $\overline{U}(x,0) = 0.05U_j$, is ≈ 6.47 for the natural and LF low-amplitude jets, ≈ 5.41 for the LW high-amplitude jet, and $\approx 5.90D$ for the HF jet. Thus, we clearly see that the LF case is more effective at modifying the mean flow than the HF one, when forcing at the same forcing amplitude. LF low-amplitude forcing results in no appreciable effect upon the turbulent mean flow. Small differences further downstream are likely associated with statistical non-convergence. Focusing on the momentum thickness, it is seen that both high-amplitude forcing cases result in a greater momentum thickness compared to the natural jet. The LF high-amplitude jet, when compared to the HF case, exhibits a rapid decrease in the centerline velocity but with a delayed increase in the momentum thickness. For the LF high-amplitude forcing case, the momentum thickness only increases substantially above the natural jet after 7D downstream. The HF forcing case results in a rapid increase in the momentum thickness, deviating from the natural jet after about 1D downstream from the nozzle lip. However, compared to the LF case, this change is confined to the shear layer region and is only evident in the centerline velocity after about $4D$.

B. Phase-locked component & boundary forced linearized Navier-Stokes results

We now examine the phase-locked component of the response as defined via the triple decomposition. This component exhibits a periodic response to the applied external forcing that is, by definition of the triple-decomposition framework, *uncorrelated* to the residual field. Figure 4 shows the phase-locked velocity magnitude for the three forced jets, corresponding to a phase, $\phi = 0$, relative to the input acoustic forcing. It is seen for the LF case, the forcing results in a large-phase locked response in the potential core region of the jet, whereas the HF case leads to a dominant phase-locked response in the near-nozzle shear layer. One can also note that the phase-locked component of the velocity magnitude is significant compared to the turbulent mean velocity. The two high-amplitude cases result in similar levels of phase-locked velocity fluctuations equal to $\approx 20\%$ of the jet velocity, similar to the velocity fluctuations present in the natural jet, while the low-amplitude forcing case results in phase-locked velocity fluctuations of about 5%.

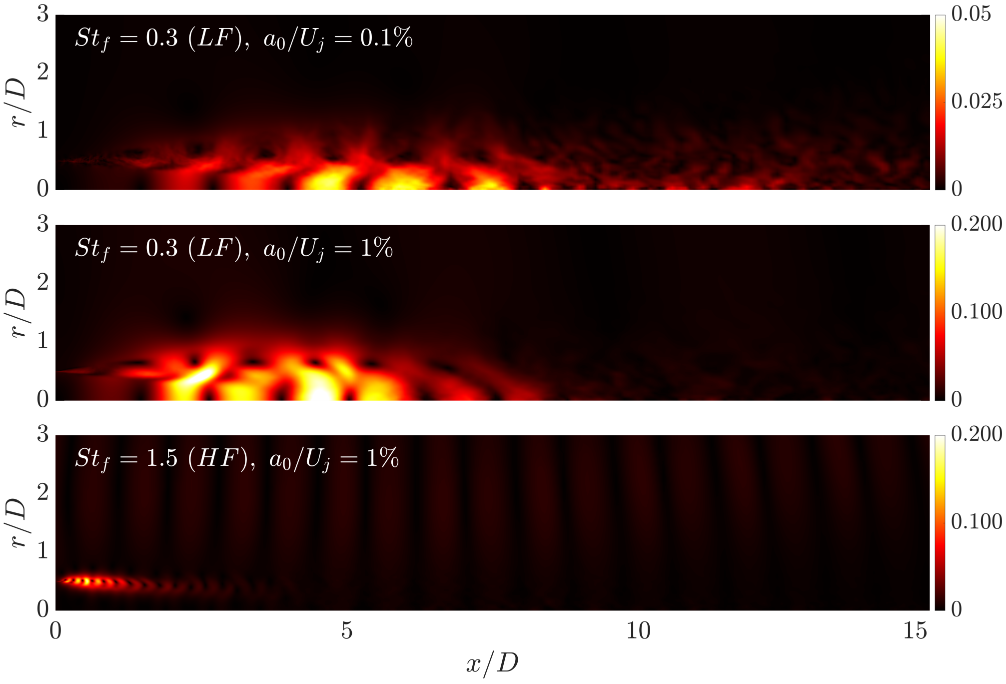

Fig. 4 Phase-locked velocity magnitude

We now compare these results to predictions based on forced LNS computations, where the mean flow used is the one measured for each different forcing case. These computations employ the linearized governing equation operator, as defined in section II.B, and the system is forced via the inlet boundary ($x = 0$). The forcing applied is the acoustic plane-wave equations and is applied to the region $r > 0.52$ to mimic the computations performed. A radius of $r > 0.52$

was chosen to avoid directly forcing the shear layer. As described in section II.B, the mean-flow eddy viscosity model from Pickering et al. [13] was employed to close the nonlinear forcing term. A single constant, $c = 0.11$, was employed for all computations.

In figure 5 we show contours of the phase-locked pressure fluctuations along with pressure contours of the LNS results for the three forced jets. At $St = 0.3$, the phase-locked response of the LF jets exhibits two primary features: the long wavelength direct acoustic waves that are unaffected by the jet along with shorter wavelength wavepackets that have been highly amplified by the jet. These are the high-amplitude structures seen in figure 4. The primary difference between the LF high-amplitude and LF low-amplitude cases is a large contraction in the wavepackets amplified by the jet. The LNS results capture all of these critical features extremely well. Both the spatial extent of the highly amplified wavepackets and the relative magnitude between these structures and the direct acoustic waves are captured well for both LF cases. At $St = 1.5$, a similar response is observed, where direct acoustic waves are accompanied by highly-amplified wavepackets in the jet, this time located in the near-nozzle shear layer. The LNS results match the phase-locked results well, capturing the correct spatial extent of the modes in the shear layer. The LNS results predict a slightly higher amplification of the wavepackets in the shear layer of the jet, thus causing the direct acoustic waves to appear weaker in the LNS contours.

The extremely close correspondence between the predicted and observed phase-locked response suggests that the phase-locked response can be predicted through only a knowledge of the (deformed) mean flow field and the inlet forcing.

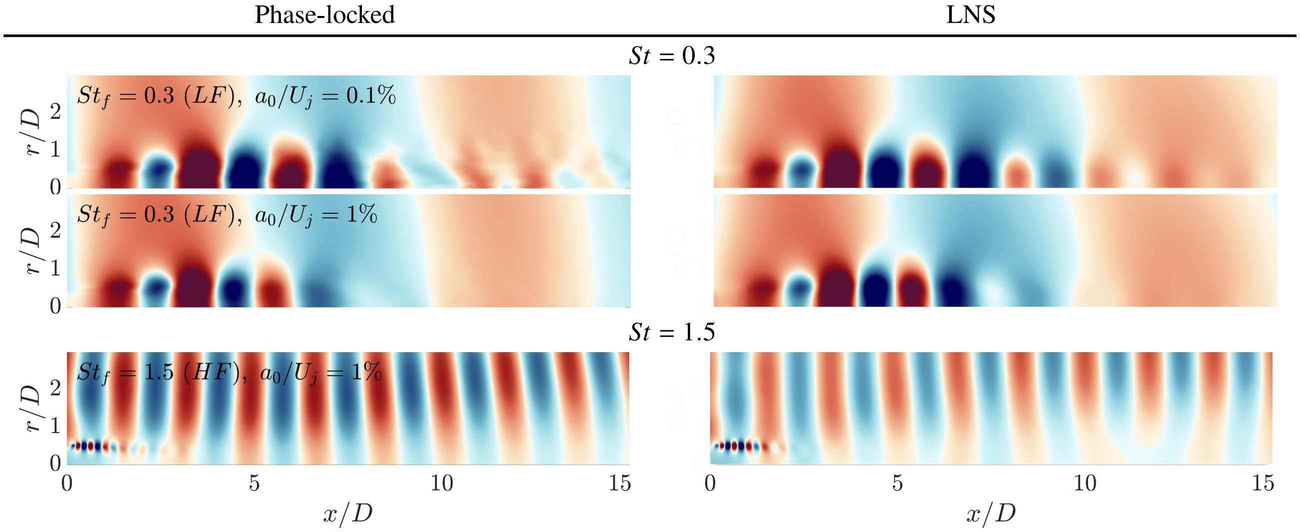

Fig. 5 Real component of the pressure fluctuations of the phase-locked component (left column) and boundary forced LNS results (right column). Contour limits: $\pm 0.5||p||_\infty$**.**

C. SPOD and resolvent analysis spectrum of the residual turbulence

We now apply SPOD to the residual component of the flow field and compare the SPOD spectrum and modes to the resolvent gain and response modes. We study how the energy and structure of the coherent modes are modified due to the applied forcing and to what extent resolvent analysis can model these changes. We focus on asymmetric disturbances, $m = 0$, for all cases due to the axisymmetric nature of the applied forcing and the underlying turbulent jet.

Figures 6, 7, and 8 show the axisymmetric, $m = 0$, SPOD eigenspectrum for the four cases considered, allowing us to compare the energy breakdown of each jet and how the energy of each mode is affected due to the forcing. Figure 6 employs the standard Reynolds decomposition, while figures 7 and 8 employ the triple decomposition framework introduced in section II.D. Essentially, this means that figure 6 presents the eigenspectrum of SPOD performed on the total fluctuating component (the residual + phase-locked components), whilst figures 7 and 8 are performed only on the residual component as defined via the triple decomposition framework. A smaller ΔSt is employed for figure 6,

$\Delta St = 0.0125$, to resolve the highly amplified peaks whilst $\Delta St = 0.05$ is employed for the triply decomposed results to improve convergence and reduce noise in the eigenspectrum. Additionally, figure 6 displays the eigenspectrum associated with the most energetic mode, whilst figures 7 and 8 display the eigenspectrum of the two most energetic modes. This allows one to observe how low-rank the jet is. Across all cases, the Hamming window is employed to minimize spectral leakage, and an overlap equal to half the block size is employed. The reader is referred to Schmidt and Colonius [25] for details about the implementation of SPOD.

Observable in figure 6 are large peaks in the energy spectrum at the forcing frequency and harmonics of the forcing frequency for both high-amplitude cases. This shows that strong nonlinear interactions have occurred for both of these cases. The LF low-amplitude forced jet has a single peak in the energy spectrum at $St = St_f$, suggesting that the jet responded in purely a linear manner to the forcing. At these frequencies, the jet exhibits low-rank behavior due to the overwhelming domination of the phase-locked response on the fluctuations present in the jet. The peaks in the energy spectrum, corresponding to the phase-locked motion, are several orders of magnitude greater than the remaining turbulence. This helps motivate employing the triple decomposition framework. In figures 7 and 8, we see that the triple decomposition has removed the peaks in the spectrum at the forcing frequency and the harmonics. This allows one to study the effect of the forcing upon the turbulence spectrum in the forced jets without contamination from the strong phase-locked component.

By examining the triply decomposed energy spectrum, the natural jet shows a low-rank response (gain separation between the dominant and subdominant mode) in a range of frequencies from about $St = 0.2$ to $St = 1.2$, with maximal gain separation around $St = 0.6$. These modes correspond to Kelvin-Helmholtz wavepackets as shown in previous work [6]. For the LF low-amplitude case, we see a slight suppression of the KH gain, but we suspect that this is not statistically significant. By contrast, for the LF high-amplitude case, we see a significant suppression of the KH wavepackets from about $St = 0.4$ on, but an amplification of them in the range $St = 0.15$ to $St = 0.4$, with a peak gain separation shifted down to $St = 0.3$. Finally, for the HF case, there is again suppression of the KH response for all frequencies up to about $St = 0.6$. This is followed by an amplification, compared to the natural jet, with a peak gain around $St \approx 0.75$. A similar peak was observed around $St = 0.88$ in the experimental study of Samimy et al. [19] when forcing a supersonic at $St_f = 1.5$. Outside of these low rank-regions, for all forced jets, it is rather remarkable how the eigenspectra are almost indistinguishable between the forced and natural cases.

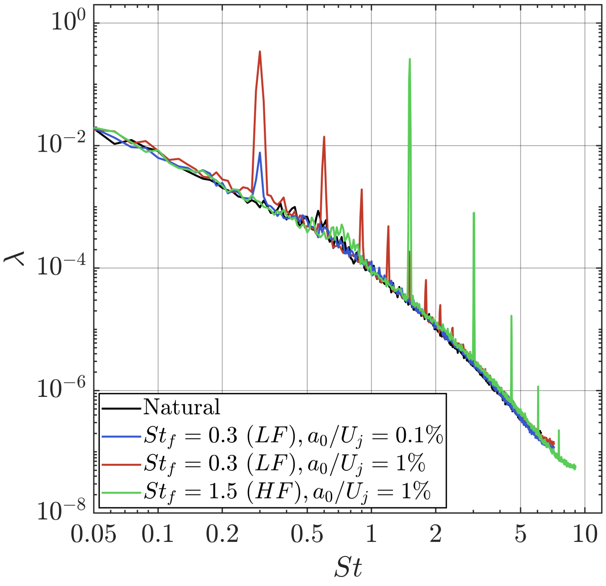

Fig. 6 SPOD λ spectrum, Reynolds decomposition, $m = 0$, $\Delta St = 0.0125$. Only the dominant modes are shown.

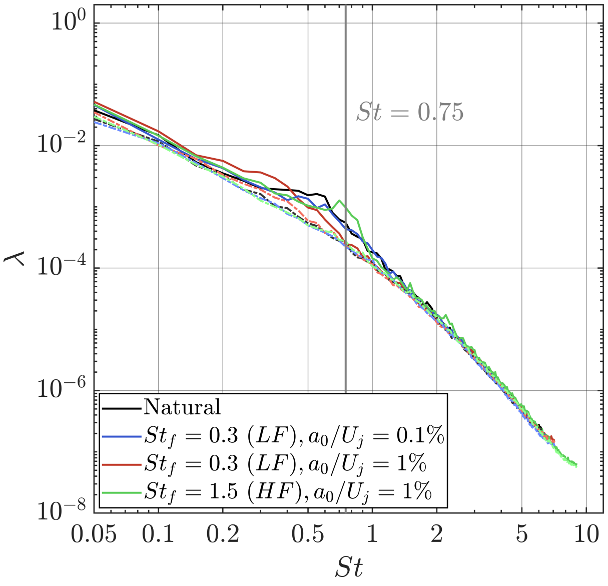

Fig. 7 SPOD λ spectrum, triple decomposition, $m = 0$, $\Delta St = 0.05$. Solid lines are the dominant modes, dashed lines are the first sub-dominant modes.

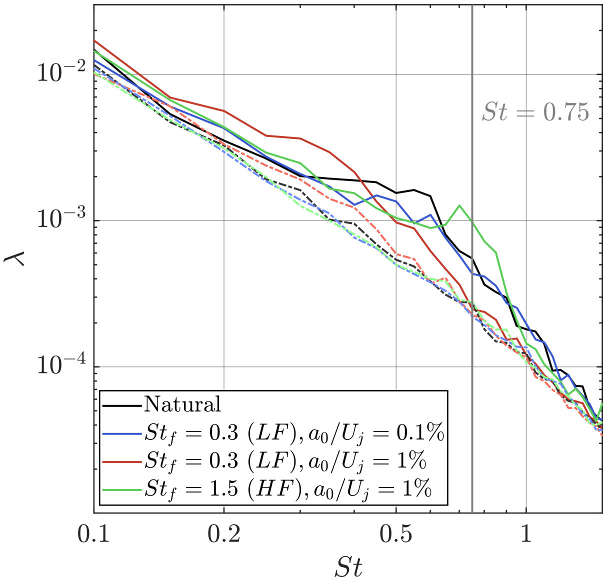

Fig. 8 Magnified version of figure 7.

Next, we compare the gain spectrum produced by the resolvent analysis and compare it to the SPOD energy spectrum. As with the LNS results, the mean-flow consistent eddy-viscosity model was employed and a single constant, $c = 0.11$ was employed for all cases considered. The gain spectrum is interesting and helps us interpret the SPOD spectra of the residual components. We see minimal change in the gain for the LF low-amplitude case, consistent with what was observed in the spectrum. For the LF high-amplitude case, we see a shift between suppression and amplification of gain compared to the natural around $St = 0.25$, with significant suppression from $St = 0.25$ on. Thus, the shift in the peak gain to lower frequencies observed in the spectrum appears to be attributable to changes to the mean flow–the more rapid decay of the centerline velocity suppresses KH instability at higher frequencies while amplifying it at lower frequencies.

We note frequency associated with the crossover between amplification and suppression is different in the resolvent gain than in the observed spectra. Of course, resolvent gain and spectra are not directly comparable, as the resolvent gain must be multiplied by the corresponding forcing amplitude to obtain the actual disturbance level. A second issue is that, at least in the natural jet, $St = 0.25$ is, at least for $m = 0$, the frequency where the dominant amplification mechanism shifts from an Orr-type mode, dominant for $St < 0.25$, to the KH mode, dominant for $St > 0.25$. A more detailed analysis of the resolvent forcing would be required to address this issue.

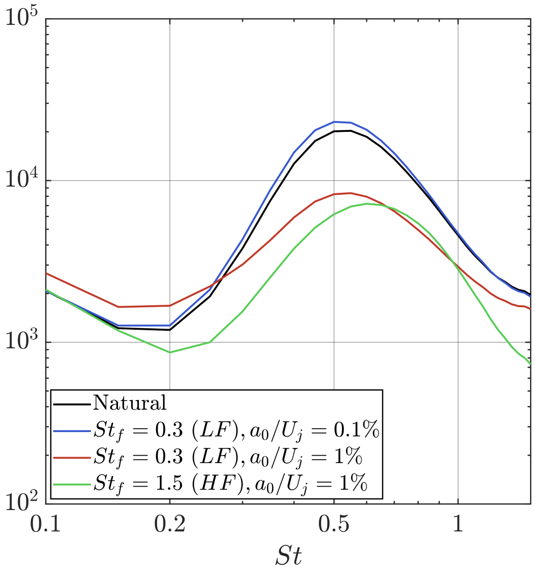

Fig. 9 Resolvent analysis gains

Turning to the HF case, we see, remarkably, a suppression of gain over all frequencies with a slight shift of the peak gain to $St = 0.6$. Compared to the LF case, the suppression is more significant over most frequencies, with rough parity of the range from $St = 0.6 \rightarrow 1$. This gain suppression seems to be related to the rapid increase in the shear-layer thickness associated with the HF case. What is most striking is the complete absence of any gain amplification around $St = 0.75$ that we might have expected based on the SPOD spectra. We hypothesize that the observed peak at $St = 0.75$ is due to a genuinely nonlinear effect, by which we mean an affect on the residual turbulence that is not attributable to the change in mean flow. In this case, we believe that the observed peak is due to vortex pairing that is intermittently occurring to the phase-locked structures at $St_f = 1.5$.

Figure 10 displays the pressure contours of the axisymmetric, $m = 0$, most energetic SPOD mode, along with the corresponding optimal resolvent mode at four frequencies for the natural and high-amplitude jets. The LF low-amplitude case is not shown as it is almost identical to the natural jet, seen via almost identical turbulent mean flows and SPOD spectra. The SPOD modes are all computed based on the residual component as defined via the triple decomposition framework. Thus, when considering the modes at the corresponding forcing frequencies, these are coherent structures that are *uncorrelated* with the imposed forcing. All cases follow the trends seen in the natural jet and correspond to KH responses [6]. As the frequency is increased, the modes become more localized to the near-nozzle shear layer. Overall, we observe qualitatively similar structures between the natural and forced jets. Starting with the $St = 0.3$ response, we see a significant contraction in the length of the wavepacket for the LF high-amplitude case and only a slightly more compact wavepacket for the HF case. Compared to $St = 0.3$, smaller contractions are seen in both high-amplitude forcing cases at $St = 0.6$.

At $St = 1$, for the LF high-amplitude case, the downstream portion of the wavepacket has formed into an Orr-type mode instead of a KH-type mode. This agrees with the energy spectrum at this frequency, where the energy gap between the optimal and sub-optimal mode has almost been eliminated for the LF high-amplitude forced jet. Thus, it appears the KH-mode has been suppressed enough such that the Orr mode is beginning to show up in the most energetic SPOD mode. For the HF jet, a significant contraction in the dominant mode is observed. At $St = 1.5$, some slightly greater differences are seen in the SPOD modes. As at previous frequencies, the LF high-amplitude case exhibits a contraction in the mode length compared to the natural jet. However, the HF case exhibits an extended KH mode, extending to the end of the potential core. Additionally, strong acoustic waves around $x/D = 15$ are present. These acoustic waves are traveling downstream and, by definition, are not phase-locked with the forcing.

At both low and high frequencies, periodic forcing has a minimal effect upon the energy spectrum and the most energetic modes present in a jet. For high-amplitude forcing, small changes to the energy spectrum are observed in the range of frequencies where the natural jet is low-rank ($St \approx 0.2 - 1.0$). However, the remainder of the spectrum remains unchanged. Minimal changes in the optimal SPOD modes were observed at the relevant frequencies. The optimal SPOD modes remained unchanged in type (KH or Orr), with only a contraction in the spatial length of the mode taking place in the high-amplitude forcing cases.

Next, we compare the resolvent analysis modes and determine to what degree they predict the results observed in SPOD. Overall, we see that resolvent analysis predicts the shifts in the modes extremely well. For all frequencies, resolvent analysis captures the large contraction seen in the LF high-amplitude SPOD modes and estimates the overall size of the mode well. One exception is at $St = 1$, where the resolvent mode captures the first KH-type wavepacket contained in the shear layer but does not capture the second Orr-type wavepacket downstream. This is likely due to the small gain separation seen in the SPOD eigenspectrum, thus resulting in the Orr-type mode to show. Whilst, the resolvent analysis modes, due to the large gain separation typically seen between the optimal and sub-optimal mode at this frequency [6, 13], only picks up on the KH-type mode. For the HF case, resolvent analysis again captures the trends in the dominant SPOD mode well. One exception is at $St = 1.5$, where resolvent analysis predicts a mode highly localized to the early shear layer of the jet. Although this is a key feature in the SPOD mode, resolvent does not capture the more downstream component in the wavepacket nor the acoustic waves in the far-field.

Overall, we see that the resolvent analysis performed on the new turbulent mean low captures the modes well. We see that resolvent analysis captures the general trend seen in the SPOD eigenspectrum for the LF high-amplitude jet. Changes to the most energetic SPOD modes and the SPOD eigenspectrum are replicated well by the resolvent analysis performed on the new turbulent mean flow. We believe that this indicates minimal interaction between the phase-locked structures and the residual component in the LF jet, resulting in resolvent analysis predicting the most energetic modes and SPOD eigenspectrum well. Resolvent analysis performed on the turbulent mean of the HF jet, again, largely capture the trends seen in the SPOD modes, except at $St = 1.5$ where significant discrepancies are present. Additionally, a remarkable reduction in the resolvent gain is seen across all frequencies with a shift in the peak gain to $St = 0.6$. However, no gain amplification is observed at $St \approx 0.75$ as is observed in the SPOD eigenspectrum. Thus, we believe that in the HF case, the interaction between the phase-locked structures and residual turbulence occurs in the form of vortex pairing, resulting in a reduced ability for resolvent analysis to predict changes to the most amplified modes and gain spectrum.

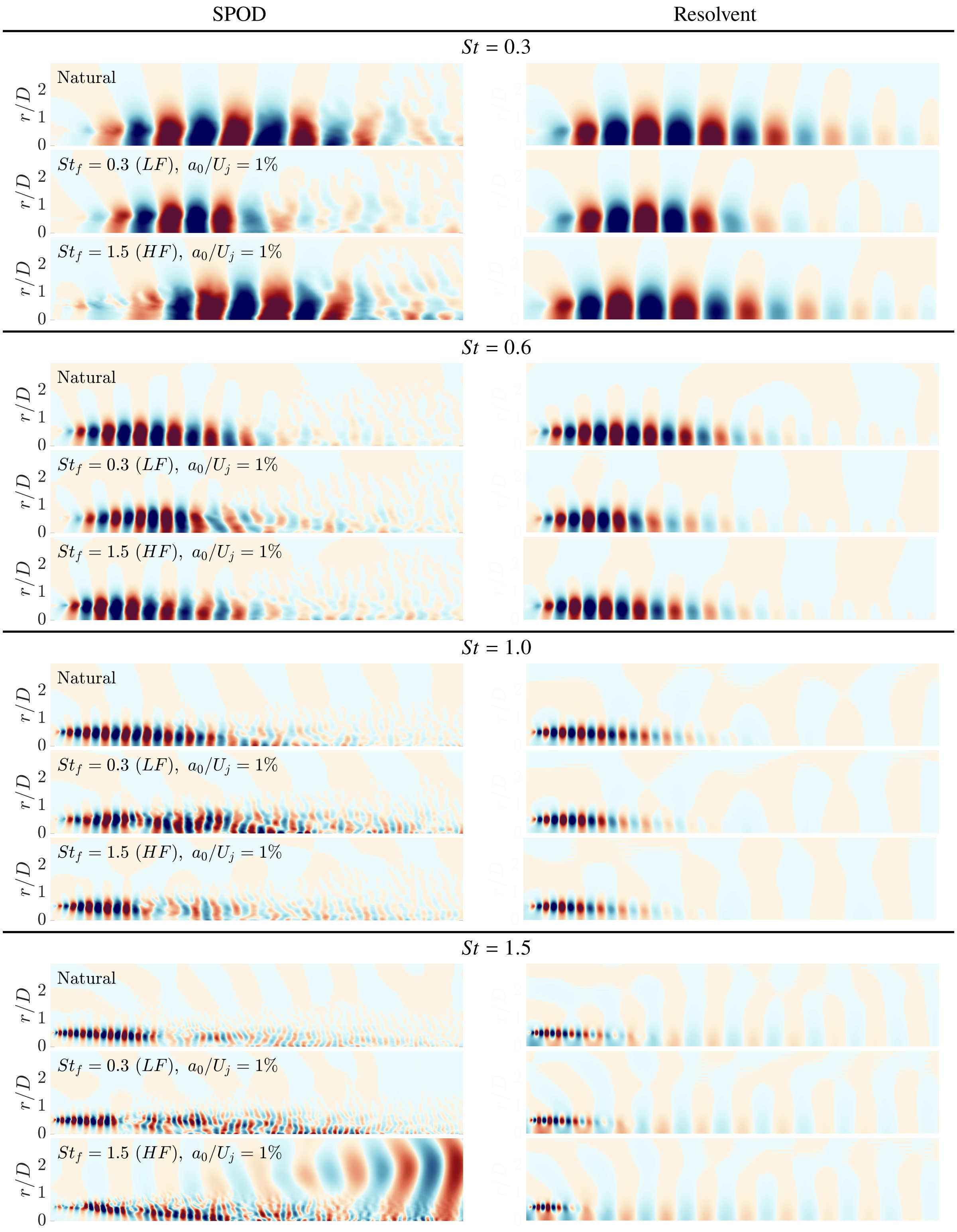

Fig. 10 **Real component of the pressure fluctuations of the dominant SPOD mode based on the residual field as defined via the triple decomposition framework (left column). Real component of the pressure component of the optimal resolvent analysis mode (right column). Contour limits: $\pm 0.5||p||_\infty$.**

IV. Summary and conclusions

Existing literature has suggested that periodic forcing is only beneficial to turbulent jet noise reduction to the extent that the forcing results in deformation to the turbulent mean flow. However, a detailed study investigating the mechanisms present by which periodic forcing alters the turbulent has been lacking. We investigated this phenomenon by performing large-eddy simulations of turbulent axisymmetric jets subjected to periodic forcing. Two forcing frequencies were investigated; a LF forcing corresponding to the jet-preferred mode [16] and a HF forcing that corresponds to forcing that previous studies [18, 19] have shown results in broadband noise reduction.

LF forcing produces highly energetic tones at the forcing frequency, and for the high-amplitude case, at several harmonics, suggesting strong nonlinear interactions. HF forcing, like LF forcing, produces a series of highly energetic tones at the forcing frequency and several harmonics. Modest changes to the mean-flow were observed in both high-amplitude cases, whereas forcing at a low-amplitude had a negligible effect upon the turbulent mean flow.

The triple decomposition framework was employed to separate the response of the jet into its turbulent mean component, a phase-locked component, and a residual component that is, on average, uncorrelated to the phase-locked component. The phase-locked component was shown to be significant, up to 20% of the jet velocity for the high-amplitude forcing cases and 5% for the low-amplitude case. The phase-locked response was compared to boundary forced LNS computation based on the new turbulent mean flow. For all jets, the LNS computations predicted this phase-locked response extremely well, both in terms of the structure but also the relative magnitude between the direct acoustic waves and the wavepackets amplified by the jet.

Despite the large amplitude of the phase-locked structures, we observed modest changes to the turbulence spectra for all cases. The LF high-amplitude case results in a shift of the peak energy corresponding to the KH wavepackets from $St \approx 0.6$ in the natural jet to $St \approx 0.3$ for the forced jet. The shift resulted from a suppression in the KH mode strength for $St > 0.4$ but an amplification of it for $St < 0.4$. The shifts in amplification of the KH mode for this case are qualitatively predicted by the resolvent gain spectrum–which showed a crossover between amplification and suppression at a lower frequency of $St = 0.25$. The HF jet also showed suppression up to about $St = 0.6$, but a sharp amplification in the energy spectrum at $St \approx 0.75$, corresponding to the first sub-harmonic frequency. This region of amplified response is completely absent from the corresponding resolvent gain spectrum, and we believe it is the result of intermittent vortex pairing of the phase-locked structures at $St_f = 1.5$.

Additionally, we observe a contraction in the dominant SPOD modes across a range of frequencies for the two high-amplitude cases. This is again consistent and well predicted by the corresponding optimal resolvent modes. Two exceptions are seen at $St = 1$ for the LF case where, due to the small energy separation between the dominant mode and sub-dominant, the Orr-type wavepacket appeared in the dominant mode. For the HF jet at this frequency, strong downstream acoustic waves and an extended KH mode is observed.

Our results largely confirm conclusions drawn from two earlier studies [2, 7], namely that while the jet is strongly receptive to unsteady forcing, it produces a phase-locked response that has a modest impact on the turbulent mean flow, but that does not result in any significant reorganization of the natural turbulence. The excellent ability of resolvent analysis and LNS to predict the most energetic modes and phase-locked structures suggests limited interaction between the phase-locked structures and the natural turbulence. An exception to this occurs in the HF forcing case. The phase-locked response at $St = 1.5$ seemed to interact with the background turbulence, resulting in intermittent vortex pairing observed around $St = 0.75$ in the SPOD spectra and is entirely absent from the corresponding mean-flow-predicted resolvent gain spectrum. Future work includes momentum and energy budgets to measure directly the interactions between phase-locked and residual turbulence. Once confirmed, we believe that the presented framework can be fruitfully employed to seek effective forcing strategies based principally on optimizing the deformation to the mean flow field.

Acknowledgments

The authors would like to thank Dr. Ethan Pickering for many productive discussions on topics related to this paper. This work has been supported by the Office of Naval Research under grant N00014-20-1-2311. The simulations presented here used the Extreme Science and Engineering Discovery Environment (XSEDE), which is supported by National Science Foundation grant number CTS-120005.

References

[1] Casalino, D., Diozzi, F., Sannino, R., and Paonessa, A., "Aircraft noise reduction technologies: a bibliographic review," Aerospace Science and Technology, Vol. 12, No. 1, 2008, pp. 1–17.

[2] Kœnig, M., Sasaki, K., Cavalieri, A. V., Jordan, P., and Gervais, Y., "Jet-noise control by fluidic injection from a rotating plug: linear and nonlinear sound-source mechanisms," Journal of Fluid Mechanics, Vol. 788, 2016, pp. 358–380.

[3] McKeon, B., and Sharma, A., "A critical-layer framework for turbulent pipe flow," J. FluidMech, Vol. 658, 2010, p. 336382.

[4] Jeun, J., Nichols, J. W., and Jovanović, M. R., "Input-output analysis of high-speed axisymmetric isothermal jet noise," Physics of Fluids, Vol. 28, No. 4, 2016, p. 047101.

[5] Jovanovic, M. R., and Bamieh, B., "Componentwise energy amplification in channel flows," Journal of Fluid Mechanics, Vol. 534, 2005, p. 145.

[6] Schmidt, O. T., Towne, A., Rigas, G., Colonius, T., and Brès, G. A., "Spectral analysis of jet turbulence," Journal of Fluid Mechanics, Vol. 855, 2018, pp. 953–982.

[7] Sinha, A., Towne, A., Colonius, T., Schlinker, R. H., Reba, R., Simonich, J. C., and Shannon, D. W., "Active control of noise from hot supersonic jets," AIAA Journal, Vol. 56, No. 3, 2018, pp. 933–948.

[8] Lumley, J. L., "The structure of inhomogeneous turbulent flows," Atmospheric turbulence and radio wave propagation, 1967.

[9] Lumley, J. L., Stochastic tools in turbulence, Courier Corporation, 2007.

[10] Towne, A., Schmidt, O. T., and Colonius, T., "Spectral proper orthogonal decomposition and its relationship to dynamic mode decomposition and resolvent analysis," Journal of Fluid Mechanics, Vol. 847, 2018, pp. 821–867.

[11] Brès, G. A., Jordan, P., Jaunet, V., Le Rallic, M., Cavalieri, A. V., Towne, A., Lele, S. K., Colonius, T., and Schmidt, O. T., "Importance of the nozzle-exit boundary-layer state in subsonic turbulent jets," Journal of Fluid Mechanics, Vol. 851, 2018, pp. 83–124.

[12] Brès, G., Jordan, P., Colonius, T., Le Rallic, M., Jaunet, V., and Lele, S., "Large eddy simulation of a Mach 0.9 turbulent jet," 2014.

[13] Pickering, E., Rigas, G., Schmidt, O. T., Sipp, D., and Colonius, T., "Optimal eddy viscosity for resolvent-based models of coherent structures in turbulent jets," Journal of Fluid Mechanics, Vol. 917, 2021.

[14] Pickering, E., Rigas, G., Nogueira, P. A. S., Cavalieri, A. V. G., Schmidt, O. T., and Colonius, T., "Lift-up, Kelvin–Helmholtz and Orr mechanisms in turbulent jets," Journal of Fluid Mechanics, Vol. 896, 2020, p. A2. https://doi.org/10.1017/jfm.2020.301.

[15] Brès, G. A., Ham, F. E., Nichols, J. W., and Lele, S. K., "Unstructured large-eddy simulations of supersonic jets," AIAA journal, Vol. 55, No. 4, 2017, pp. 1164–1184.

[16] Crow, S. C., and Champagne, F. H., "Orderly structure in jet turbulence," Journal of Fluid Mechanics, Vol. 48, No. 3, 1971, p. 547–591. https://doi.org/10.1017/S0022112071001745.

[17] Mair, M., Bacic, M., Chakravarthy, K., and Williams, B., "Jet preferred mode vs shear layer mode," Physics of Fluids, Vol. 32, No. 6, 2020, p. 064106.

[18] Samimy, M., Kim, J.-H., Kastner, J., Adamovich, I., and Utkin, Y., "Active control of a Mach 0.9 jet for noise mitigation using plasma actuators," AIAA journal, Vol. 45, No. 4, 2007, pp. 890–901.

[19] Samimy, M., Kim, J.-H., Kearney-Fischer, M., and Sinha, A., "Acoustic and flow fields of an excited high Reynolds number axisymmetric supersonic jet," Journal of Fluid Mechanics, Vol. 656, 2010, pp. 507–529.

[20] Chu, B.-T., "On the energy transfer to small disturbances in fluid flow (Part I)," Acta Mechanica, Vol. 1, No. 3, 1965, pp. 215–234.

[21] Sirovich, L., "Turbulence and the dynamics of coherent structures. I. Coherent structures," Quarterly of applied mathematics, Vol. 45, No. 3, 1987, pp. 561–571.

[22] Aubry, N., "On the hidden beauty of the proper orthogonal decomposition," Theoretical and Computational Fluid Dynamics, Vol. 2, No. 5-6, 1991, pp. 339–352.

[23] Schmid, P. J., "Dynamic mode decomposition of numerical and experimental data," Journal of fluid mechanics, Vol. 656, 2010, pp. 5–28.

[24] Semeraro, O., Jaunet, V., Jordan, P., Cavalieri, A. V., and Lesshafft, L., "Stochastic and harmonic optimal forcing in subsonic jets," 22nd AIAA/CEAS Aeroacoustics Conference, 2016, p. 2935.

[25] Schmidt, O. T., and Colonius, T., "Guide to spectral proper orthogonal decomposition," AIAA journal, Vol. 58, No. 3, 2020, pp. 1023–1033.

[26] Hussain, A. K. M. F., and Reynolds, W. C., "The mechanics of an organized wave in turbulent shear flow," Journal of Fluid Mechanics, Vol. 41, No. 2, 1970, pp. 241–258.

[27] Hussain, A., and Reynolds, W., "The mechanics of an organized wave in turbulent shear flow. Part 2. Experimental results," Journal of Fluid Mechanics, Vol. 54, No. 2, 1972, pp. 241–261.

[28] Reynolds, W., and Hussain, A., "The mechanics of an organized wave in turbulent shear flow. Part 3. Theoretical models and comparisons with experiments," Journal of Fluid Mechanics, Vol. 54, No. 2, 1972, pp. 263–288.

[29] Bogey, C., and Bailly, C., "Influence of nozzle-exit boundary-layer conditions on the flow and acoustic fields of initially laminar jets," Journal of Fluid Mechanics, Vol. 663, 2010, pp. 507–538.